



Geometrical quality inspection in 3D concrete printing using AI-assisted computer vision

Weiji Cui · Wenliang Liu · Ruyi Guo · Da Wan ·
Xiaona Yu · Luchuan Ding · Yaxin Tao

Received: 27 August 2024 / Accepted: 30 January 2025 / Published online: 14 February 2025
© The Author(s) 2025

Abstract 3D concrete printing is an innovative technology poised to transform the construction industry by enabling the automated, layer-by-layer creation of structures directly from digital models. This approach offers numerous advantages over traditional construction methods, including reduced labor costs, faster build times, and the ability to produce complex geometries with high precision. However, unlike conventional mold-cast concrete, 3D printable

concrete must support itself without external formwork, posing significant challenges related to material deformation during the printing process. Uncontrolled deformation can lead to structural instability, design deviations, and cumulative errors. Traditional methods for monitoring the geometrical quality of 3D-printed concrete are often insufficient in accuracy and efficiency. Recent advancements in artificial intelligence (AI) present new opportunities for addressing these challenges. AI-assisted methods leverage machine learning to analyze large datasets, enabling more accurate predictions and real-time monitoring and control of deformation during the 3D printing process. In this paper, we explored the application of AI-assisted methods for real-time deformation analysis in 3D concrete printing. Specifically, the Yolo-v5 algorithm, an AI-assisted object detection technique, was employed for the computer vision of extruded concrete filaments. Several quantitative metrics were proposed, including the layer height, layer angle, and curvature. In addition, the rheological properties of 3D-printed concrete were measured to refine the computer vision analysis results. Through experimental validation, we demonstrated the effectiveness of the developed AI-assisted computer vision system in monitoring the 3D concrete printing process.

W. Cui · W. Liu · R. Guo
Department of Civil Engineering, Qingdao University of Technology, Qingdao, China

W. Cui
Intelligent Construction Lab, Qingdao University of Technology, Qingdao, China

R. Guo
Lixia Experimental Primary School, Jinan, China

D. Wan
School of Architecture, Tianjin Chengjian University, Tianjin, China

X. Yu
Weifang Engineering Vocational College, Weifang, China

L. Ding
College of Civil Engineering, Tongji University, Shanghai, China

Y. Tao (✉)
Institute of Building Materials, ETH Zurich, Zurich, Switzerland
e-mail: yaxtao@ethz.ch

Keywords 3D concrete printing · Geometrical quality inspection · Computer vision · Artificial intelligence · Image analysis



1 Introduction

3D concrete printing, a novel and rapidly evolving technology, stands at the forefront of modern construction innovation [1, 2]. This cutting-edge technique involves using automated machines to deposit layers of concrete based on digital models, bypassing the need for traditional formwork and labor-intensive processes. As such, 3D concrete printing presents a paradigm shift with far-reaching implications for the construction industry [3]. The advantages of 3D concrete printing are manifold. Firstly, it significantly reduces labor costs by automating the construction process, thus minimizing the need for manual labor [4]. Furthermore, 3D concrete printing allows for accelerated construction timelines. By streamlining the building process, structures can be completed in a fraction of the time required by conventional methods [5]. Another compelling benefit is the ability to create complex and customized geometries with the potential to reach unprecedented precision. However, the high precision requires more means of performance evaluation and quality control [6].

Despite the above-mentioned advantages, the processing of 3D printable concrete differs fundamentally from conventional mold-cast concrete, presenting unique challenges. In traditional construction, mold-cast concrete is poured into formwork that provides external support until the material gains sufficient strength. This formwork acts as a mold, shaping the concrete and preventing deformation. However, in 3D concrete printing, there is no external support; the extruded material must support itself from the moment it is deposited. This self-supporting requirement introduces a range of issues related to the deformation of the extruded concrete [7]. The deformation of extruded material must be meticulously controlled to ensure structural integrity and dimensional accuracy. If deformation is not adequately managed, several disadvantages can arise. One major issue is the potential for the printed layers to sag or collapse under their weight, leading to compromised structural stability [8–10]. Additionally, excessive deformation can result in deviations from the intended design, causing misalignment and irregularities in the final structure. In addition to deformation control, the extrudability of 3D printable concrete is a critical factor influencing the quality and success of the printing process. Poor extrudability can result in

significant tearing or discontinuities in the extruded filament, severely compromising the overall print quality and structural performance. Extrudability is highly dependent on the mixture design of the concrete, with key factors being the particle size and volume fraction of the aggregates [11, 12]. The size of the aggregates must be carefully controlled to ensure smooth extrusion through the nozzle without causing blockages or inconsistencies in the flow. Similarly, the volume fraction of aggregates plays a vital role; too high a fraction can lead to clogging and reduced cohesiveness of the mix, while too low a fraction may result in a weak structure that cannot adequately support subsequent layers [13].

To address these challenges, various methods have been developed for the data acquisition of the deformation of extruded material in 3D concrete printing. One approach is 3D laser scanning, particularly terrestrial laser scanning (TLS), which has become widely adopted for generating precise 3D point clouds in various engineering disciplines [14]. Its primary benefits include high accuracy, the capability to measure over long distances, and minimal reliance on typical atmospheric conditions, especially lighting [15, 16]. Nonetheless, it does have some drawbacks, such as sensitivity to material reflectivity, high costs, detail level dependent on the distance from the object, limited portability, and challenges in operating in crowded environments. Additionally, noise from moving equipment and personnel on construction sites can affect data quality [17, 18]. Another advanced technology is structured light scanning (SLS), which is among the most utilized optical 3D measurement methods due to its straightforward implementation and rapid full-field data acquisition. The technique projects sinusoidal patterned light onto a surface, which is captured and processed by a camera to triangulate pixel coordinates, forming a point cloud [19]. The primary advantages of this method include quick scanning times, high resolution, and minimal reliance on the material properties, texture, or lighting conditions. Unfortunately, this technology is limited to relatively small objects that are positioned close to the projector [20, 21]. Photogrammetry remains the most used and affordable measurement method. The widespread use of affordable digital cameras has led to a significant increase in the number of photos taken daily on construction sites. Regarding 3D printing of concrete, Miranda

et al. [22] quantified the deformation of printed concrete layers experimentally by extracting the layer height manually from images. A similar approach was also adopted by Ashrafi et al. [23]. Barjuei et al. [24] proposed a real-time vision-based control framework capable of regulating layer width by automatically adjusting the printing velocity based on the tracked layer contour against a black background. Photogrammetry offers the benefit of more continuous sampling compared to laser scanning, though the pixel size can be a limiting factor. However, this method faces challenges such as sensitivity to varying lighting conditions, particularly when dealing with harsh shadows, low-textured surfaces, and windows. Therefore, it is necessary to develop a method that can automatically and efficiently detect deformations in 3D-printed concrete from complex images.

In recent years, the advent of artificial intelligence (AI) has introduced new possibilities for analyzing and controlling deformation in 3D concrete printing. AI-assisted methods leverage machine learning algorithms to analyze vast amounts of data and identify patterns that may not be apparent through traditional approaches. One significant advantage of AI-assisted methods is their ability to process and learn from large datasets, enabling more accurate and reliable predictions of deformation behavior from complex images [25]. Several studies have already demonstrated the potential of AI-assisted deformation analysis in 3D printing. For instance, 2D image data have been utilized as feedback to enable continuous monitoring and automatic adjustment of 3D-printing parameters, improving 3D printing quality [26]. Lao et al. [27] applied a machine learning technique to correlate the formation of the extrudate to the printing parameters and successfully predicted the extrudate geometry to find proper nozzle shapes. A layer-by-layer continuous quality monitoring system was developed for 3D printing, which involved comparing sample images with real-time print images [28]. Any differences were analyzed using control charts to monitor the printing process layer by layer. Additionally, machine learning techniques have been employed to predict surface roughness. In cases where defects such as nozzle blockages or layer misalignments are critical, machine learning methods have been implemented to detect these issues [29]. Since the performance of parts produced through additive manufacturing is heavily influenced

by processing parameters, AI-assisted techniques can help optimize these parameters for improved quality [30]. In addition, Silva et al. [31] focused on a specific aspect of machine learning, called speed control, which regulates layer width by adjusting the robot motion speed or material flow rate to avoid defects and deviations. A similar approach has been adopted in other research to characterize the local geometry and texture of the layers and to detect the defects of printed filaments [32–35]. However, previous studies failed to effectively address the challenge of identifying interlayer lines in complex backgrounds, limiting their applicability in diverse printing scenarios. Furthermore, they often overlooked the development of multiple indices for the quantification of layer geometry, which are crucial for assessing filament quality. This study bridges these gaps by not only introducing comprehensive geometric indices but also correlating them with rheological properties.

In this paper, specifically, we build on these advances by exploring the application of AI-assisted methods for real-time deformation analysis and control in 3D concrete printing. We employed the Yolo v5 algorithm for extruded filament recognition to address the challenge of identifying interlayer lines with complex backgrounds, aiming to achieve automatic recognition of interlayer lines and lay a foundation for their quantification [36]. Python was used to develop the code, incorporating both OpenCV and U-Net for the extraction of crucial parameters related to the quality of extruded filaments, including the layer height, layer angle, and curvature. The geometric quality of the extruded filaments was analyzed, and a correlation analysis was conducted in conjunction with rheological properties. The relationship between the quantified metrics and rheological properties was summarized, and the applicability of the quantification methods was evaluated.

2 Experimental program

2.1 Materials and sample preparation

The binder comprises cement (fast-hardening P42.5 type), Grade II fly ash (FA), slag, and silica fume (SF). Manufactured sand, with a maximum particle size of 9.50 mm, was classified into three fineness categories, including 2.5, 2.9, and 3.3. Viscosity modifying



admixture (VMA) was used to improve the shape stability of 3D-printed concrete. Furthermore, Superplasticizer (SP) was utilized to regulate the extrudability of 3D-printed concrete. The water-to-binder ratio was 0.35 for all mixtures. Three different levels of binder-to-sand ratios (b/s) were considered (0.6, 0.8, and 1), and the mixture design of 3D-printed concrete is listed in Table 1. Note that the adjustments in admixtures were conducted as preliminary experiments to regulate the material's extrusion properties, ensuring the material meets the minimum requirements for extrudability. The materials were prepared using a JJ-5 cement mortar mixer with a 1-L capacity for rheological testing and a UJZ-15 concrete mixer with a 15-L capacity for extrusion testing.

2.2 Testing procedures

2.2.1 Stress growth tests

Static yield stress of 3D-printed concrete was determined using stress growth tests with an eBT-V concrete rheometer (Schleibinger, Germany). The process began with loading fresh material in a container with a diameter of 244 mm and a volume of 20 L. After ensuring the rheometer was properly calibrated, the vane was rotated with a constant speed of 0.5 rpm for a total period of 180 s. The radius and height of the blades were 52.5 mm and 103 mm, respectively. The maximum torque measured during the whole procedure was used to calculate the static yield stress, as shown in the following equation.

$$\tau = \frac{T}{2\pi R^2 H} \quad (1)$$

where T is the torque (N·m), R and H are the radius and height of blades (m).

2.2.2 Flow curve measurements

Flow curve measurements were also carried out using the eBT-V concrete rheometer. The testing protocol commenced with a gradual increase in rotational speed from 0 to 30 rpm over the initial 10 s. After this preliminary ramp-up phase, the procedure included six additional steps, each featuring a 5-rpm reduction in rotational speed. Each step was held for 10 s to ensure stable measurements of torque and rotational speed. The test was repeated twice for each mixture. The measured torques and rotational speeds in the descent stage was fit, following Eq. (2).

$$T = G + HN \quad (2)$$

where T is the torque in N·m, G is the intercept in N·m, H is the slope in Nm·s, and N is the rotational speed in rpm.

The Reiner-Riwlin equations were applied to the raw data to obtain the yield stress and plastic viscosity, as in Eq. (3) and Eq. (4).

$$\tau_0 = \frac{\left(\frac{1}{R_1^2} - \frac{1}{R_2^2}\right)}{4\pi h \ln\left(\frac{R_2}{R_1}\right)} G \quad (3)$$

where τ_0 is the yield stress in Pa, R_1 is the vane radius in m, R_2 is the inner cup radius in m, h is the vane height in m.

$$\mu = \frac{\left(\frac{1}{R_1^2} - \frac{1}{R_2^2}\right)}{8\pi^2 h} H \quad (4)$$

Table 1 Mixture design of 3D-printed concrete (kg/m³)

No	b/s	Fineness	Cement	FA	Slag	SF	Water	Sand	VMA	SP
1	0.6	3.3	332.0	99.6	199.2	33.2	232.4	1106.8	1.33	5
2	0.8	3.3	373.4	112.0	224.0	37.3	261.4	933.4	1.49	5
3	1	3.3	403.5	121.1	242.1	40.4	282.4	807.0	1.61	5
4	0.6	2.9	332.0	99.6	199.2	33.2	232.4	1106.8	1.33	5
5	0.8	2.9	373.4	112.0	224.0	37.3	261.4	933.4	1.49	5
6	1	2.9	403.5	121.1	242.1	40.4	282.4	807.0	1.61	5
7	0.6	2.5	332.0	99.6	199.2	33.2	232.4	1106.8	1.33	5
8	0.8	2.5	373.4	112.0	224.0	37.3	261.4	933.4	1.49	5
9	1	2.5	403.5	121.1	242.1	40.4	282.4	807.0	1.61	5

where μ is the plastic viscosity in Pa·s.

2.2.3 Extrusion tests

The 3D printing extrusion device consists of two main parts: the extrusion section and the detection section, as shown in Fig. 1. A screw was employed to consistently transport and extrude the material at a speed of 15 mm/s. A Logitech C930c camera with 1080p resolution was mounted 100 mm at the lateral side of the filament to capture its geometrical contours. In each group, three filaments were printed, each with a length of 350 mm and a nozzle diameter of 20 mm. The printing speed was uniformly set to 20 mm/s across all mixtures.

3 Computer vision program

3.1 Yolo-v5 neural network

Yolo-v5, which was developed by the Ultralytics team, was adopted in the current study. It is a widely used object detection algorithm comprising four main components: the input layer, backbone, neck, and head [36]. The input layer is responsible for receiving image data and performing preprocessing tasks to prepare the images for feature extraction. The backbone extracts high-level features from input images using a convolutional neural network, forming a

feature pyramid for subsequent fusion. Key components of the backbone include the Conv module, C3 module, and SPPF module. The Conv module consists of Conv2d (for convolution operations), Batch-Norm2d (for batch normalization), and the SiLU activation function (introducing nonlinearity to enhance the network's ability to learn complex tasks). The C3 module, comprising three Conv modules and a Bottleneck module, increases network depth and receptive field, thereby improving feature extraction capabilities. The SPPF module includes an initial convolution layer (for feature compression), multiple serial max-pooling operations, and a final convolution layer that fuses features of different scales. This enhances the model's ability to detect targets of varying sizes and shapes with improved accuracy. The neck integrates a Feature Pyramid Network (FPN) and a Path Aggregation Network (PAN). The FPN employs a top-down structure for upsampling lower-level feature maps, infusing them with high-level semantic information. Conversely, the PAN utilizes a bottom-up pathway for downsampling, transferring positional information. This FPN+PAN combination ensures that feature maps of varying scales incorporate rich semantic and localization information, bolstering the network's robustness and object detection capability. These enhanced features are subsequently passed to the head for prediction. The head performs the final prediction tasks, including classification and bounding box regression. It primarily consists of three 1×1

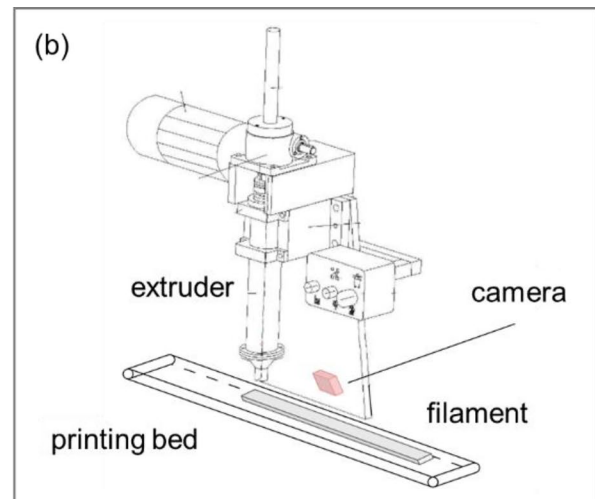


Fig. 1 Extrusion setup equipped with a digital camera: **a** real setup, and **b** schematic

convolution layers, which process high-quality feature maps from the neck to complete detection tasks.

In this study, an improved Yolo-v5 algorithm was employed for computer vision tasks, representing one of the most widely adopted object detection frameworks. The enhanced Yolo-v5 model comprises three primary components: backbone, neck, and head, as illustrated in Fig. 2. In the modified model, two attention mechanism modules have been added to the backbone, four attention mechanism modules have been incorporated into the neck, and an additional segmentation network has been introduced in the head.

3.2 Dataset processing

In this study, for each mixture proportion, multiple filaments were printed, and 100 images were collected using a high-resolution camera during the printing process, resulting in a total of 900 images. From these, 659 high-quality images were selected and subsequently divided into training and testing sets at a 4:1 ratio. The open-source image annotation tool LabelMe was employed for this task [37], allowing for the application of various annotation methods such as rectangles, polygons, and points to label the dataset. Annotations were made by drawing bounding boxes around each object or region within the images. The annotated data was then exported in XML format

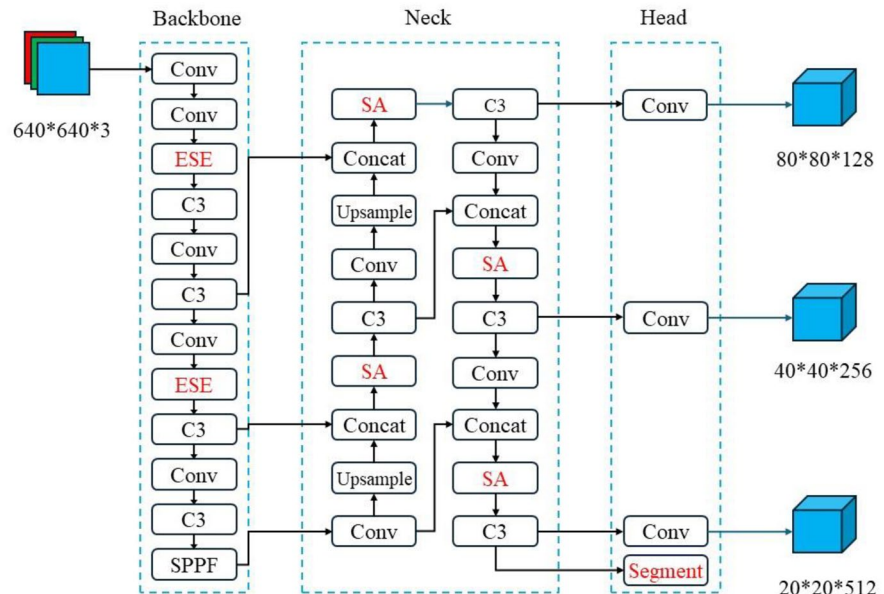
for use in training models and for labeling and categorization purposes, as depicted in Fig. 3.

The image presented is a visual representation of the dataset's annotated features and their distribution, which serves to aid in understanding the distribution and correlation of each feature within the dataset. This visualization provides a crucial foundation for subsequent steps in model training or data preprocessing.

In the top-left corner, there is a red square plot that represents the distribution of instances, specifically focusing on the distribution of concrete filaments. The entire plot is filled with red, indicating that concrete filaments constitute a significant proportion of the dataset. This complete fill implies that all instances in the dataset are concrete filaments, highlighting their dominance in the dataset. The upper right corner features a horizontal line chart, which visualizes the distribution of a specific feature within the dataset. The red lines in this chart display how this feature is distributed across different samples. The distribution shows a concentration at both the top and bottom, suggesting a pattern that resembles the outline of concrete filaments. This pattern indicates the feature's alignment with the physical characteristics of the concrete filaments.

In addition to these, several other plots depict the relationships between various features, such as x and y coordinates, width, height, and others. Each plot

Fig. 2 Improved Yolo-v5 neural network



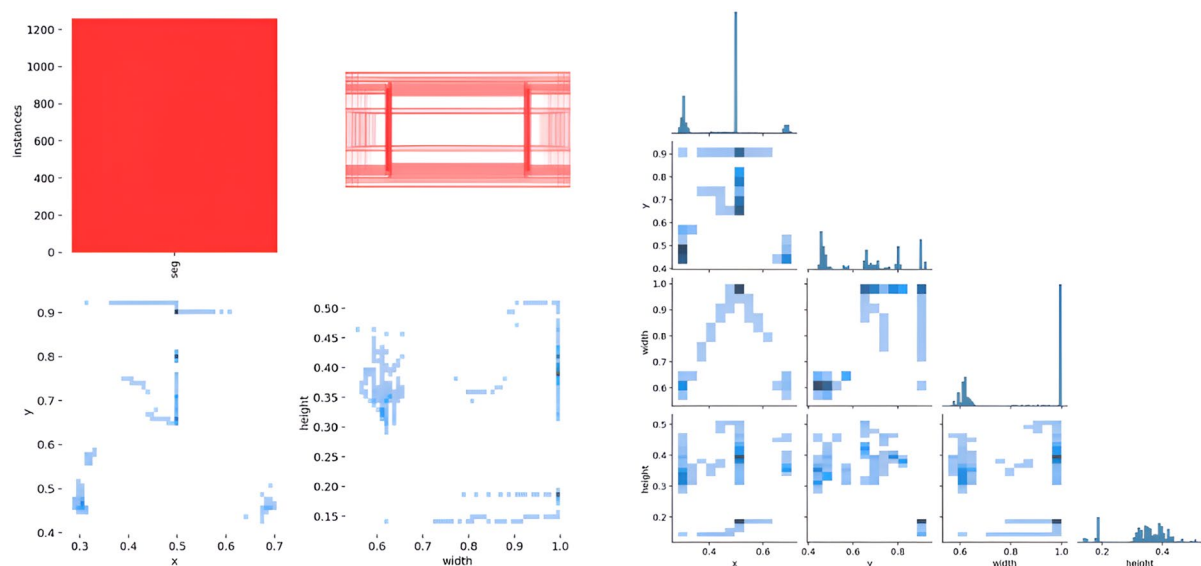


Fig. 3 Labeling categories and settings of the dataset

contains points that represent individual samples, with the color and density reflecting the quantity or distribution density of the samples. Through these visualizations, the correlations or distribution patterns between different features in the dataset become evident. This allows for a deeper analysis of how these features interrelate and contribute to the overall structure of the dataset.

The model training was carried out in an Ubuntu 20.04 environment on a system equipped with an RTX2080 GPU and 16 GB of memory. The training hyperparameters for Yolo-v5 were configured as follows: a batch size of 16, 200 epochs, a learning rate of 0.0001, a weight decay of 0.0005, and a momentum of 0.937. The batch size is set to 16, which directly affects GPU memory usage, training speed, and model performance. Larger batch size can accelerate training but may lead to insufficient GPU memory and potentially degrade model performance. Given the available GPU with 16 GB of memory, a batch size of 16 is chosen to balance training speed and model performance [38]. The number of training epochs is initially set to 200, which represents the number of complete passes through the dataset by the neural network. This number may be adjusted based on the model's performance, specifically to address overfitting or underfitting issues observed during training [39].

For the loss functions and backpropagation optimizer, ‘torch.nn.CrossEntropyLoss’ is selected as the classification loss function for the model, and Mean Squared Error (MSE) is used for regression tasks. Stochastic Gradient Descent (SGD) is chosen as the optimizer function for backpropagation, with an initial learning rate set to 0.01. A custom learning rate adjustment strategy is implemented, where a higher learning rate is used initially to accelerate model convergence, followed by a gradual reduction in the learning rate to fine-tune and find the optimal solution [38]. Weight decay is set to 0.0005, which is equivalent to L2 norm regularization. This setting reduces model complexity and helps prevent overfitting by penalizing large weights. The momentum is set to 0.937. Momentum adjustment addresses the issue of slow optimization due to small learning rates causing oscillations in SGD, thus speeding up training and improving model stability [36]. Other hyperparameters are left at their default settings.

The relationship between the number of training epochs and the regression and classification losses in the model is illustrated in Fig. 4. The key metrics for evaluating the performance of this model include bounding box loss, segmentation loss, objectness loss, classification loss, precision, recall, and mean average precision (mAP). These metrics provide a comprehensive assessment of how well the model

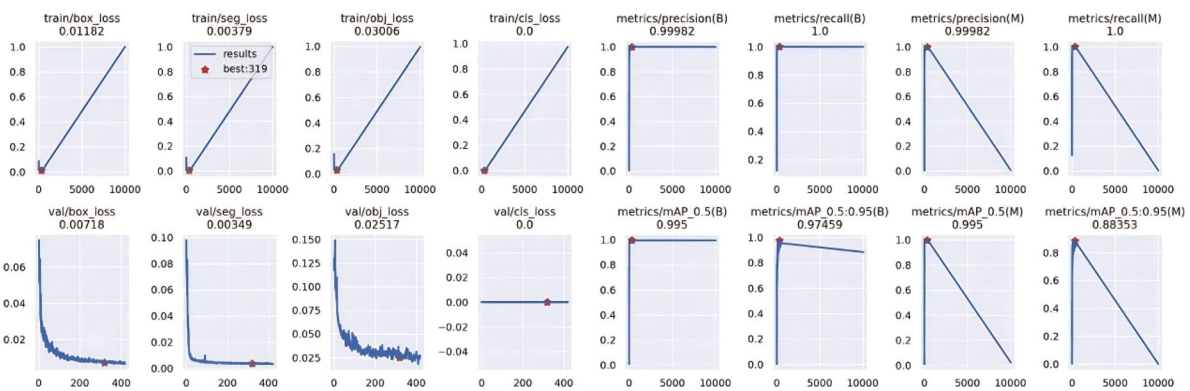


Fig. 4 The relationship between the number of training epochs and the regression and classification losses in the model

performs in various aspects of object detection and segmentation tasks.

In the upper section, which focuses on training losses and evaluation metrics, several important trends are observed. The ‘train/box_loss’ metric tracks the change in bounding box loss during training, which measures the difference between the predicted and ground truth bounding boxes. The loss reaches its minimum value of 0.01181 at epoch 207, after which an increase suggests potential overfitting of the model. Similarly, ‘train/seg_loss’ reflects the segmentation loss during training, evaluating the difference between the predicted segmentation regions and actual regions in the image segmentation task. The minimum loss of 0.00397 also occurs at epoch 207, with a subsequent rise indicating overfitting. The ‘train/obj_loss’ captures the change in objectness loss during training, assessing the model’s precision in detecting the presence of objects, with a recorded value of 0.02204. The ‘train/cls_loss’ tracks classification loss during training, showing the error in categorizing objects. The loss reaches its minimum value of 0.0 at epoch 207, signifying perfect precision in category prediction on the training data. Additionally, precision and recall metrics for both background (B) and medium-sized objects (M) provide insight into the model’s ability to correctly identify and categorize objects. Precision, represented by ‘metrics/precision’, indicates the proportion of true positives among all samples predicted as positive. A plateau in this metric suggests that precision reaches 99%, demonstrating high precision in distinguishing between background and medium-sized objects. Recall,

reflected in ‘metrics/recall’, measures the proportion of true positives among all actual positive samples, with a plateau indicating that recall reaches 100%.

The lower section focuses on validation losses and evaluation metrics, which are calculated on the validation set to assess the model’s generalization to unseen data. The ‘val/box_loss’ for the bounding box on the validation set reaches a value of 0.00585, while ‘val/seg_loss’ for segmentation is 0.00333. The ‘val/obj_loss’ for objectness on the validation set is 0.03483, and the ‘val/cls_loss’ for classification is 0.0. The ‘metrics/mAP_0.5’ metric indicates high detection precision, with a value of 0.995 for both background and medium-sized objects at an intersection over union (IoU) threshold of 0.5. The more stringent ‘metrics/mAP_0.5:0.95’ metric, averaged over IoU thresholds from 0.5 to 0.95, yields values of 0.98894 for background and 0.99496 for medium-sized objects.

The training and validation metrics suggest that the model is well-optimized. The bounding box loss and objectness loss decrease progressively during training, indicating effective learning. Precision and recall metrics approaching or reaching 1.0 show excellent performance on the training set. High mAP values on the validation set demonstrate the model’s strong generalization ability, and the close alignment between training and validation metrics suggests that the model does not exhibit significant overfitting. These results highlight the model’s effectiveness in object detection and segmentation tasks, with strong performance both on seen and unseen data.

3.3 Quantitative evaluation indices

Geometrical quality was quantified using three indices, including the layer height, the local angle, and the local curvature.

The first index is the layer height. Assuming the center point of the camera's field of view follows the printing path S_L , the layer height is calculated by the edge line S_T . The distance between the edge line points $(x_{0,i}, y_j)$ and $(x_{1,i}, y_j)$ denotes the layer height $h^k(x)$:

$$h^k(x) = \begin{cases} \sqrt{(x_{0,0} - x_{1,0})^2}, & x_0 < x < x_1 \\ \sqrt{(x_{0,1} - x_{1,1})^2}, & x_1 < x < x_2 \\ \vdots \\ \sqrt{(x_{0,m-1} - x_{1,m-1})^2}, & x_{m-1} < x < x_m \end{cases} \quad (5)$$

where k is a hyperparameter for selecting the positions for distance calculation.

The second index is the local angle. Let $S_T \subset Z^2$ represent an inter-layer line or edge line, and let $R(d, l)$ denote a line segment of length l and angle d , where $d \in [-90, 90]$. The line length is chosen to be 1/5 of the image width from the central area, where the boundary effects at both ends can be avoided. This hyperparameter balances between the available line angles and the measurement locations. Let $p \in Z^2$ be a point in the image. Then, $F(p, d) = [S_T \times R(d, 2)](p)$, represents the set S_T with a directional line d , passing through it. The orientation parameter ϕ is defined as:

$$\phi(p) = \begin{cases} \arg \max_{d \in D} F(p, d), & p \in S_T \\ \text{none} & \end{cases} \quad (6)$$

The third index represents the local curvature of the geometric contour. Local curvature quantifies the degree of smoothness of curve over a defined interval. For edge lines $S_T \subset Z^2$, use m segments of cubic spline functions $S_n(x)$ to interpolate S_T . The interpolation function $S_n(x)$ for L_n is

$$S_n = \begin{cases} s_n^1(x - x_1), & x_1 < x < x_2 \\ s_n^2(x - x_1), & x_1 < x < x_2 \\ \vdots \\ s_n^m(x - x_{m-1}), & x_{m-1} < x < x_m \end{cases} \quad (7)$$

where m is a hyperparameter that indicates the number of segments. n specifies whether the edge line of the filament is on the left (0) or right (1).

The curvature K at point x of $S_n(x)$ is:

$$K = \frac{|s'|}{(1 + s'^2)^{3/2}} \quad (8)$$

4 Results and discussion

4.1 Rheological properties of 3D-printed mixtures

The rheological properties of 3D-printed concrete are shown in Fig. 5. The data showed a clear trend where the static yield stress decreased as the binder-to-sand ratio increased. For a binder-to-sand ratio of 0.6, static yield stress ranged from 1228.96 Pa to 2001.06 Pa. In contrast, at a binder-to-sand ratio of 1, this value dropped significantly, ranging from 772.1 Pa to 929.1 Pa. This reduction suggested that a higher proportion of binder resulted in a material that required less stress to initiate flow, indicating improved ease of flow when the material was in a static state [40]. Similarly, dynamic yield stress followed a decreasing trend with an increase in the binder-to-sand ratio. For a ratio of 0.6, dynamic yield stress ranged between 298.35 Pa and 396.85 Pa. When the ratio was increased to 1, dynamic yield stress further decreased, ranging from 280.57 Pa to 338.7 Pa. Plastic viscosity also showed a significant decrease with higher binder-to-sand ratios. At a binder-to-sand ratio of 0.6, plastic viscosity ranged from 110.17 Pa·s to 152.05 Pa·s. At a ratio of 1, plastic viscosity dropped to between 60.82 Pa·s and 109.82 Pa·s. This indicated that the material became less resistant to flow under dynamic or vibratory conditions as the binder content increased, reflecting enhanced flowability under such conditions [12, 41].

Regarding the effect of the fineness modulus of aggregates, the analysis revealed a trend where static yield stress decreased as the fineness modulus decreased. For a fineness modulus of 3.3, static yield stress ranged from 929.1 Pa to 2001.06 Pa. In contrast, for a fineness modulus of 2.5, static yield stress dropped significantly, ranging from 772.1 Pa to 1228.96 Pa. Like that, the dynamic yield stress exhibited a decreasing trend with a decrease in the fineness

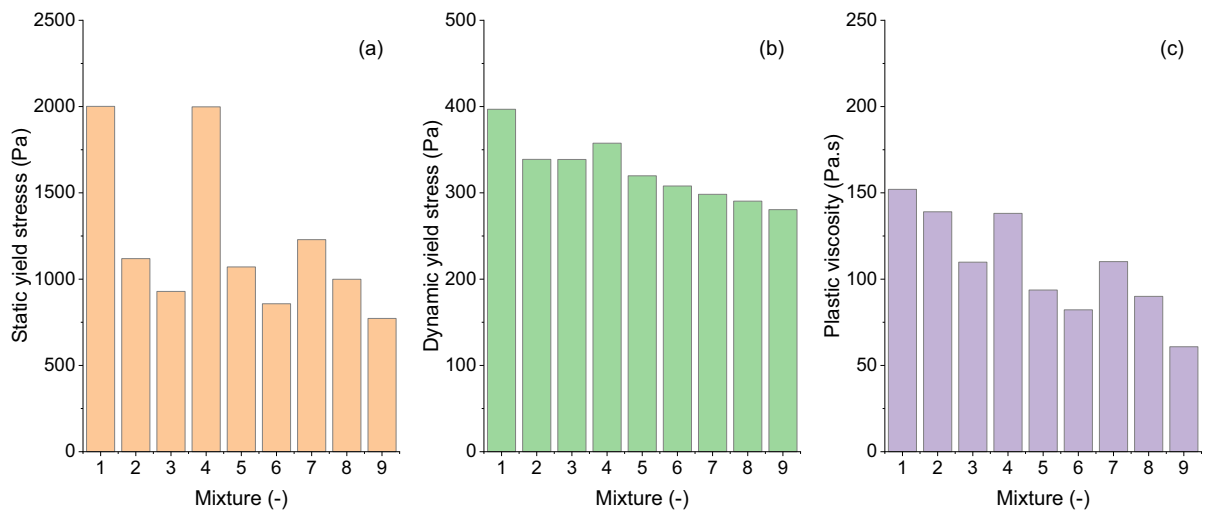


Fig. 5 Rheological properties of 3D-printed concrete: **a** static yield stress, **b** dynamic yield stress, and **c** plastic viscosity

modulus. For a fineness modulus of 3.3, dynamic yield stress ranged between 338.7 Pa and 396.85 Pa. When the fineness modulus was reduced to 2.5, dynamic yield stress further decreased, ranging from 280.57 Pa to 298.35 Pa. Plastic viscosity also demonstrated a notable decrease with lower fineness modulus values. At a fineness modulus of 3.3, plastic viscosity ranged from 109.82 Pa·s to 152.05 Pa·s. In contrast, for a fineness modulus of 2.5, plastic viscosity was lower, ranging from 60.82 Pa·s to 110.17 Pa·s. Similar results were observed in previous studies [42, 43].

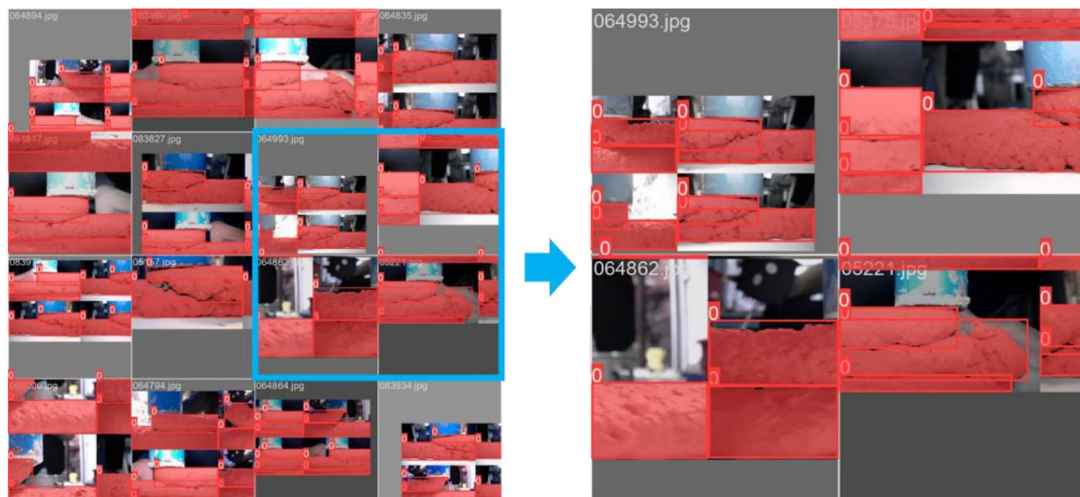
4.2 Quantification of image analysis

Figure 6 illustrates the comprehensive process of using Yolo-v5, encompassing data collection, annotation, model prediction, and result analysis. In Fig. 6a, the original image data utilized during Yolo-v5 model training is presented. These images capture ongoing 3D concrete printing scenes, clearly showcasing the features of interlayer lines. Figure 6b demonstrates the annotation process. The red rectangular boxes in the images represent the target regions marked during annotation, while the results of this process are displayed on the right side of the panel. Specific annotation details are highlighted with blue boxes, further refining the annotations. The red boxes specify the areas the model needs to focus on during training. These annotated

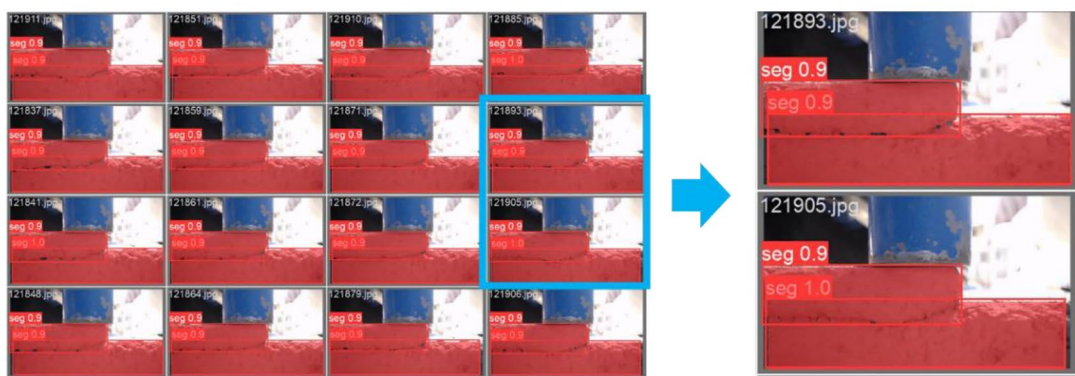
datasets are then converted into the Yolo format, which includes class labels and bounding box coordinates. In addition, in Fig. 6c, the outcomes of model predictions are shown. On the left, the red rectangular boxes indicate the target regions identified by the trained model in various images, with confidence scores (e.g., 0.9, 1.0) displayed on each box. These scores reflect the model's certainty in detecting the targets. On the right, a single image is detailed, illustrating the segmented regions and showcasing Yolo-v5's capability in both object detection and segmentation. It is evident from the figure that the model effectively segments the interlayer lines. As a follow-up, this study conducted nine experiments to analyze the images collected during the experiment, gathering various images, as shown in Fig. 7. Afterward, the geometrical contour lines were extracted from the images. By comparing the images before and after extraction, it can be concluded that the method effectively reduces noise and captures the contour lines. Note that lighting variations impact image quality by altering contrast and the visibility of interlayer lines. Strong light or reflections can cause shadows or highlights, complicating background separation, while low light introduces noise that hinders feature extraction. Even though the light conditions were not controlled constantly in the current study, the adoption of the Yolo-v5 model has proven to possess robust feature extraction capabilities, as indicated in Sect. 3.2.



(a)



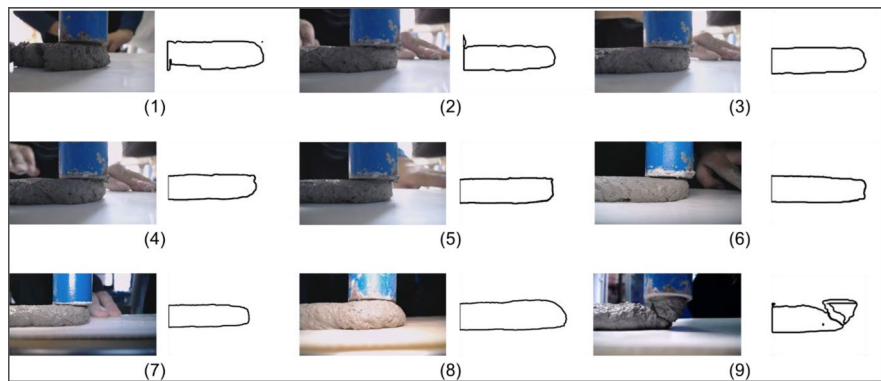
(b)



(c)

Fig. 6 The complete process of Yolo-v5: **a** original images, **b** batch training, and **c** batch testing datasets

Fig. 7 Extraction of the contour of 3D-printed filament



The quantitative results of computer vision are shown in Fig. 8. The data analysis revealed that both the binder-to-sand ratio and fineness modulus significantly impacted the height of 3D-printed concrete. Increasing the binder-to-sand ratio generally led to lower print heights. For example, with a fineness modulus of 2.5, increasing the binder-to-sand ratio resulted in reduced heights, dropping from 9.03 mm to 8.01 mm. The local angle, which influences the material's structural orientation, generally decreased as the binder-to-sand increased. For example, with a fineness modulus of 3.3, the local angle decreased from 8.54° at a binder-to-sand ratio of 0.6 to 7.56° at a ratio of 1. This trend suggested that as the binder content increased, the material exhibited a more uniform orientation or alignment, resulting in a lower local angle. However, with a fineness modulus of 2.9,

the local angle decreased from 5.23° at a binder-to-sand ratio of 0.6 to 4.54° at a ratio of 1, except at a binder-to-sand ratio of 0.8, where it peaked at 7.23°. Curvature, which quantified the smoothness of a curve by indicating the degree of fluctuation within a given range, showed varied patterns depending on the binder-to-sand ratio and fineness modulus. For a fineness modulus of 3.3, curvature decreased from 0.132 mm^{-1} at a binder-to-sand ratio of 0.6 to 0.048 mm^{-1} at a ratio of 0.8 before slightly increasing to 0.081 mm^{-1} at a ratio of 1.

4.3 Correlation with rheological properties

The height of the extrusion filament can reflect the print quality of the concrete filament from the vertical dimension. The variations in the extrusion filament

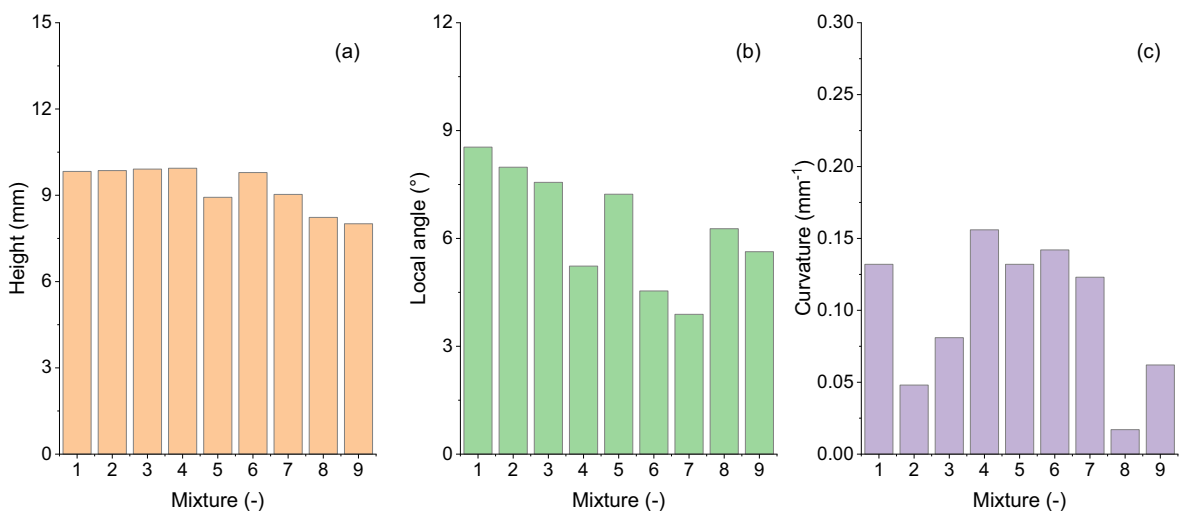


Fig. 8 Quantitative results of computer vision: **a** height, **b** local angle, and **c** curvature

height with changes in rheological properties are shown in Fig. 9. As observed from the figure, in general, the increase in static yield stress, dynamic yield stress, or plastic viscosity improves the height of one 3D-printed concrete filament. Specifically, as static yield stress increases, the material's ability to withstand its own weight and external forces improves, which is essential for maintaining the intended height and shape of each printed layer [9, 44]. This property is particularly important when constructing taller structures, where the cumulative weight of the layers can otherwise lead to sagging or collapse if the yield stress is insufficient [45].

Additionally, dynamic yield stress plays a crucial role during the extrusion process. A higher dynamic yield stress means the concrete can resist flow under the mechanical stress applied during printing, allowing for more precise deposition and reducing the risk of spreading or flattening that can compromise layer height. This resistance to flow ensures that each layer maintains its designed dimensions, contributing to the overall accuracy and uniformity of the printed structure. Moreover, high plastic viscosity helps maintain the concrete's shape immediately after extrusion, preventing layers from merging or losing their definition [46].

Despite the observed trends, the fitting performance between the rheological parameters and the variations in filament height was not satisfactory. This

discrepancy can be attributed to the complex and non-linear interactions between the material properties, extrusion process, and environmental factors. Specifically, in this study, the deformation patterns were influenced by factors beyond the rheological parameters alone, such as nozzle design, extrusion speed, and environmental conditions like temperature and humidity. The inherent variability in the extrusion process also contributes to the poor fitting results. For instance, minor fluctuations in extrusion pressure or inconsistencies in material homogeneity can lead to significant variations in filament height that are not solely governed by static yield stress, dynamic yield stress, or plastic viscosity. These findings suggest that while rheological parameters are critical for understanding the behavior of 3D printable concrete, they cannot fully explain the deformation behavior of extruded filaments in isolation. Therefore, the developed machine learning model to better monitor the deformation during the printing process provides a significant approach.

4.4 Validation

For practical engineering applications, three distinct scenarios were developed using images of real extruded filaments, as illustrated in Fig. 10. The visual inspection indicated that the printing quality differed among the cases, with Case 2 appearing to be of

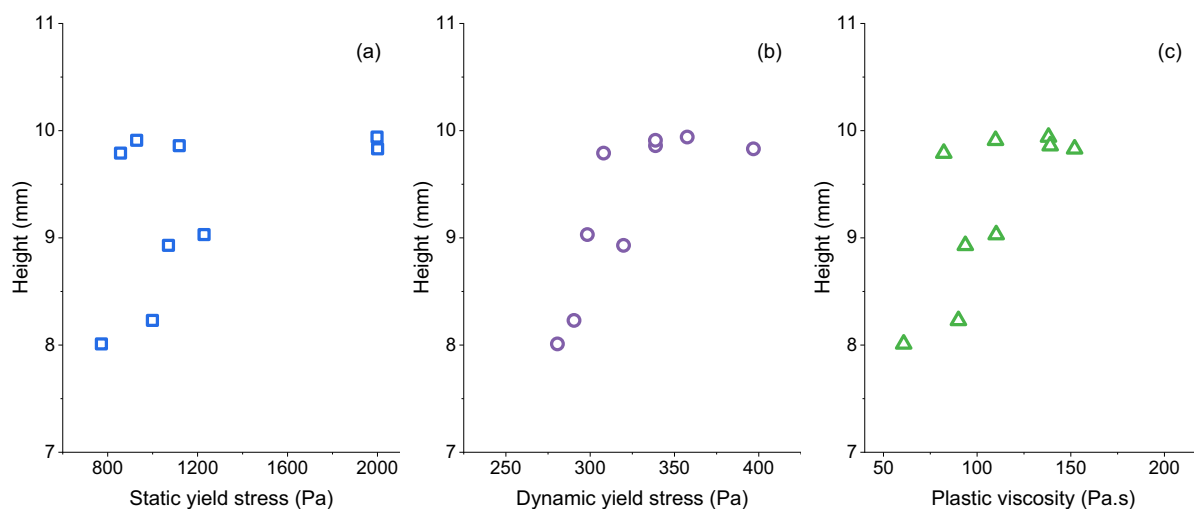


Fig. 9 Variation in layer height with changes in rheological properties: **a** static yield stress, **b** dynamic yield stress, and **c** plastic viscosity

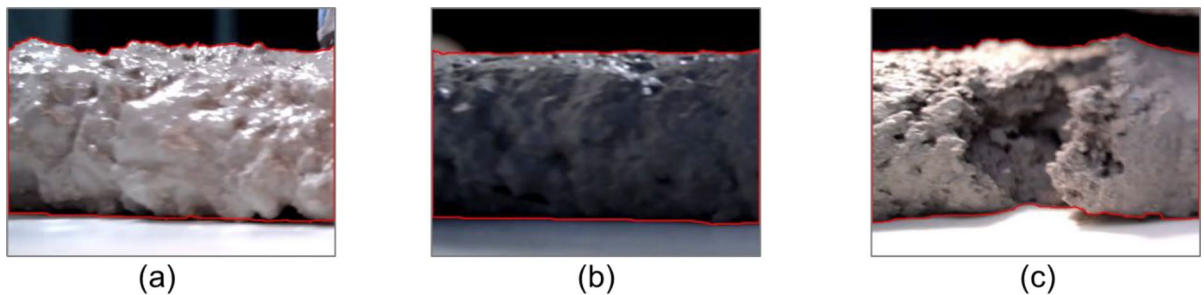


Fig. 10 3D-printed filaments with different quality levels: **a** Case 1; **b** Case 2, and **c** Case 3

higher quality compared to Case 1 and Case 3, though these differences could not be precisely quantified through visual observation alone. Consequently, this section utilized the previously mentioned quantitative methods to assess and analyze the filament quality more accurately.

The analysis aimed to ensure that the filament edges remained close to horizontal, defining an acceptable angle range as $(-10, 10)$ degrees. The ideal layer thickness was 10 mm, with an acceptable range of $(9, 11)$ mm. Based on the extracted contours, a quantitative analysis was conducted on the obtained data, including filament height and local angle. The statistical analyses were visualized through histograms, as shown in Figs. 11 and 12. To convert pixel points, the process began with the total number of points (in the thousands). The relative frequency was then determined by dividing the count of points for each specific index by the total number of points. Results indicated that, for Cases b and c, the height met the design requirements. However, for Case a,

the height did not meet the requirements. Regarding the angle parameter, Case b was essentially compliant with the specifications, whereas Cases a and c did not meet the requirements.

5 Conclusions

The paper investigates how AI-assisted techniques, specifically the Yolo-v5 algorithm for object detection, can enhance the real-time analysis and control of deformation during the 3D concrete printing process, focusing on metrics like layer height, layer angle, and curvature. The researchers also measured the rheological properties of the concrete to refine the computer vision analysis. Based on the experimental investigations and model analysis, the following conclusions can be drawn:

- (1) The annotated data was used for training with specific hyperparameters, such as a batch size of

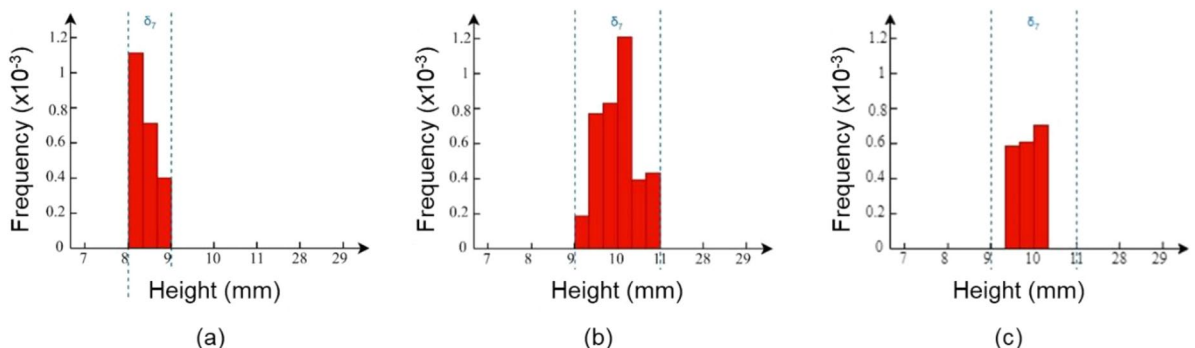


Fig. 11 Histograms of statistical analysis of height: **a** Case 1; **b** Case 2, and **c** Case 3

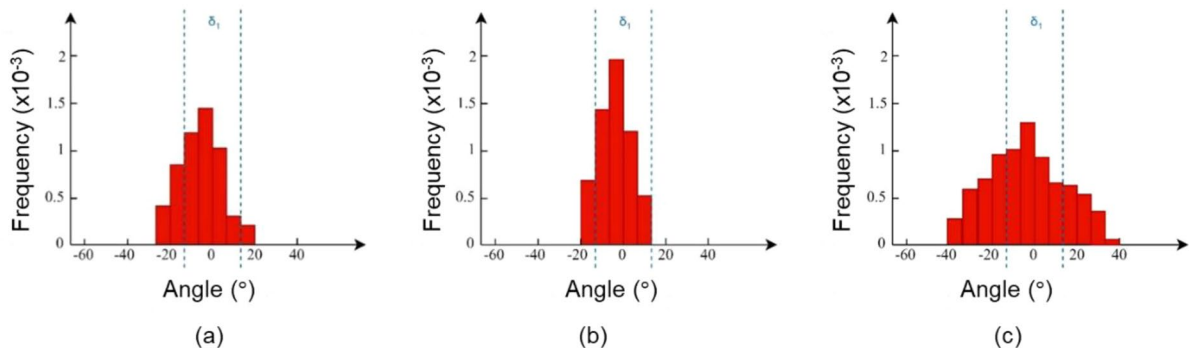


Fig. 12 Histograms of statistical analysis of local angle: **a** Case 1; **b** Case 2, and **c** Case 3

16 and 200 epochs. The model's performance, evaluated through various metrics like bounding box loss and mean average precision, showed excellent accuracy and generalization. High precision and recall values on both the training and validation sets indicate that the model is well-optimized and effective in object detection and segmentation tasks, without significant overfitting.

- (2) Visual and quantitative analyses of real extruded filaments confirm that the combination of optimal binder-to-sand ratios and fineness modulus significantly affects print quality. Increasing the binder-to-sand ratio decreases both static and dynamic yield stresses and plastic viscosity, enhancing the flowability and ease of extrusion of the concrete. Lower fineness modulus (finer aggregates) leads to reduced yield stresses and plastic viscosity, improving the mixture's flow characteristics. The best results were observed in Case 2, aligning well with design specifications for height and angle, whereas Cases 1 and 3 exhibited various levels of non-compliance.

Acknowledgements The authors acknowledge the financial support provided by the National Natural Science Foundation of China (Nos. 52008224), the Open Fund of the Institute for Sustainable Marine Architecture Research and Technological Innovation (iSMART) grant number 2019GSF110004 of Qingdao University of Science and Technology (Nu. 2020-031), the Key Technology Research and Development Program of Shandong Province (grant number 2019GSF110004), and the ETH Zurich Postdoctoral Fellowship (23-2 FEL-059). The authors thank Prof. Jian Gong from Shanghai Construction Group

Co. Ltd for providing the testing equipment and insightful suggestions.

Funding Open access funding provided by Swiss Federal Institute of Technology Zurich.

Data availability All data, models, and code generated or used during the study appear in the submitted article.

Open Access This article is licensed under a Creative Commons Attribution 4.0 International License, which permits use, sharing, adaptation, distribution and reproduction in any medium or format, as long as you give appropriate credit to the original author(s) and the source, provide a link to the Creative Commons licence, and indicate if changes were made. The images or other third party material in this article are included in the article's Creative Commons licence, unless indicated otherwise in a credit line to the material. If material is not included in the article's Creative Commons licence and your intended use is not permitted by statutory regulation or exceeds the permitted use, you will need to obtain permission directly from the copyright holder. To view a copy of this licence, visit <http://creativecommons.org/licenses/by/4.0/>.

References

1. Khoshnevis B (2004) Automated construction by contour crafting—related robotics and information technologies. Automat Constr 13:5–19. <https://doi.org/10.1016/j.autcon.2003.08.012>
2. Gosselin C, Duballet R, Roux P, Gaudilli  re N, Dirrenberger J, Morel P (2016) Large-scale 3D printing of ultra-high performance concrete: a new processing route for architects and builders. Mater Des 100:102–109. <https://doi.org/10.1016/j.matdes.2016.03.097>
3. De Schutter G, Lesage K, Mechtherine V, Nerella VN, Habert G, Agusti-Juan I (2018) Vision of 3D printing with concrete: technical, economic and environmental

- potentials. *Cem Concr Res* 112:25–36. <https://doi.org/10.1016/j.cemconres.2018.06.001>
4. Ma G, Buswell R, Leal da Silva WR, Wang L, Xu J, Jones SZ (2022) Technology readiness: a global snapshot of 3D concrete printing and the frontiers for development. *Cem Concr Res* 156:106774. <https://doi.org/10.1016/j.cemconres.2022.106774>
 5. Rollakanti CR, Prasad CVSR (2022) Applications, performance, challenges and current progress of 3D concrete printing technologies as the future of sustainable construction: a state of the art review. *Mater Today*. <https://doi.org/10.1016/j.matpr.2022.03.619>
 6. Lloret-Fritschi E, Wangler T, Gebhard L, Mata-Falcón J, Mantellato S, Scotto F, Burger J, Szabo A, Ruffray N, Reiter L, Boscaro F, Kaufmann W, Kohler M, Gramazio F, Flatt R (2020) From smart dynamic casting to a growing family of digital casting systems. *Cem Concr Res* 134:106071. <https://doi.org/10.1016/j.cemconres.2020.106071>
 7. Roussel N (2018) Rheological requirements for printable concretes. *Cem Concr Res* 112:76–85. <https://doi.org/10.1016/j.cemconres.2018.04.005>
 8. Suiker ASJ, Wolfs RJM, Lucas SM, Salet TAM (2020) Elastic buckling and plastic collapse during 3D concrete printing. *Cem Concr Res* 135:106016. <https://doi.org/10.1016/j.cemconres.2020.106016>
 9. Chen Y, Zhang Y, He S, Liang X, Schlangen E, Çopuroğlu O (2023) Improving structural build-up of limestone-calcined clay-cement pastes by using inorganic additives. *Constr Build Mater* 392:131959. <https://doi.org/10.1016/j.conbuildmat.2023.131959>
 10. Muthukrishnan S, Ramakrishnan S, Sanjayan J (2021) Technologies for improving buildability in 3D concrete printing. *Cem Concr Comps* 122:104144. <https://doi.org/10.1016/j.cemconcomp.2021.104144>
 11. Ren Q, Tao Y, Jiao D, De Schutter G, Jiang Z (2022) Rheological properties of concrete with manufactured sand: a multi-level prediction. *Cem Concr Comps* 133:104647. <https://doi.org/10.1016/j.cemconcomp.2022.104647>
 12. Mohan MK, Rahul AV, Van Tittelboom K, De Schutter G (2021) Rheological and pumping behaviour of 3D printable cementitious materials with varying aggregate content. *Cem Concr Res* 139:106258. <https://doi.org/10.1016/j.cemconres.2020.106258>
 13. Shantanu B, Smrati J, Manu S (2023) Criticality of binder-aggregate interaction for buildability of 3D printed concrete containing limestone calcined clay. *Cem Concr Comps* 136:104853. <https://doi.org/10.1016/j.cemconcomp.2022.104853>
 14. Arayici Y (2007) An approach for real world data modelling with the 3D terrestrial laser scanner for built environment. *Automat Constr* 16:816–829. <https://doi.org/10.1016/j.autcon.2007.02.008>
 15. Bosché F (2010) Automated recognition of 3D CAD model objects in laser scans and calculation of as-built dimensions for dimensional compliance control in construction. *Adv Eng Inform* 24:107–118. <https://doi.org/10.1016/j.aei.2009.08.006>
 16. Gordon Stuart J, Lichti Derek D (2007) Modeling terrestrial laser scanner data for precise structural deformation measurement. *J Surveying Eng* 133:72–80. [https://doi.org/10.1061/\(ASCE\)0733-9453\(2007\)133:2\(72\)](https://doi.org/10.1061/(ASCE)0733-9453(2007)133:2(72))
 17. Omar T, Nehdi ML (2016) Data acquisition technologies for construction progress tracking. *Automat Constr* 70:143–155. <https://doi.org/10.1016/j.autcon.2016.06.016>
 18. R. Buswell, P. Kinnell, J. Xu, N. Hack, H. Kloft, M. Maboudi, M. Gerke, P. Massin, G. Grasser, R. Wolfs (2020) Inspection methods for 3D concrete printing, Second RILEM International Conference on Concrete and Digital Fabrication: Digital Concrete, Springer, 790–803
 19. Wi K, Suresh V, Wang K, Li B, Qin H (2020) Quantifying quality of 3D printed clay objects using a 3D structured light scanning system. *Addit Manuf* 32:100987. <https://doi.org/10.1016/j.addma.2019.100987>
 20. Niven L, Steele TE, Finke H, Gernat T, Hublin J-J (2009) Virtual skeletons: using a structured light scanner to create a 3D faunal comparative collection. *J Archaeol Sci* 36:2018–2023. <https://doi.org/10.1016/j.jas.2009.05.021>
 21. Shanley C, Obertová Z, Franklin D (2024) Dimensional accuracy of structured light scans and 3D prints of various human skeletal elements. *Forensic Sci Int* 361:112138. <https://doi.org/10.1016/j.forsciint.2024.112138>
 22. de Miranda LRM, Jovanović B, Lesage K, De Schutter G (2023) Geometric conformability of 3D Concrete printing mixtures from a rheological perspective. *Materials*. <https://doi.org/10.3390/ma16216864>
 23. Ashrafi N, Duarte JP, Nazarian S, Meisel NA (2019) Evaluating the relationship between deposition and layer quality in large-scale additive manufacturing of concrete. *Virtual Phys Prototyping* 14:135–140. <https://doi.org/10.1080/17452759.2018.1532800>
 24. Shojaei Barjuei E, Courteille E, Rangeard D, Marie F, Perrot A (2022) Real-time vision-based control of industrial manipulators for layer-width setting in concrete 3D printing applications. *Adv Industrial Manufact Eng* 5:100094. <https://doi.org/10.1016/j.aime.2022.100094>
 25. Yao X, Lyu X, Sun J, Wang B, Wang Y, Yang M, Wei Y, Elchalakani M, Li D, Wang X (2023) AI-based performance prediction for 3D-printed concrete considering anisotropy and steam curing condition. *Constr Build Mater* 375:130898. <https://doi.org/10.1016/j.conbuildmat.2023.130898>
 26. Jin Z, Zhang Z, Gu GX (2019) Autonomous in-situ correction of fused deposition modeling printers using computer vision and deep learning. *Manufacturing Letters* 22:11–15. <https://doi.org/10.1016/j.mfglet.2019.09.005>
 27. Lao W, Li M, Wong TN, Tan MJ, Tjahjowidodo T (2020) Improving surface finish quality in extrusion-based 3D concrete printing using machine learning-based extrude geometry control. *Virtual and Physical Prototyping* 15:178–193. <https://doi.org/10.1080/17452759.2020.1713580>
 28. Najjartabar Bisheh M, Chang SI, Lei S (2021) A layer-by-layer quality monitoring framework for 3D printing. *Comput Industrial Eng* 157:107314. <https://doi.org/10.1016/j.cie.2021.107314>
 29. Wu D, Wei Y, Terpenny J (2019) Predictive modelling of surface roughness in fused deposition modelling using data fusion. *Int J Prod Res* 57:3992–4006. <https://doi.org/10.1080/00207543.2018.1505058>

30. Nasiri S, Khosravani MR (2021) Machine learning in predicting mechanical behavior of additively manufactured parts. *J Market Res* 14:1137–1153. <https://doi.org/10.1016/j.jmrt.2021.07.004>
31. Silva JM, Wagner G, Silva R, Morais A, Ribeiro J, Mould S, Figueiredo B, Nóbrega JM, Cruz PJS (2024) Real-time precision in 3D concrete printing: controlling layer morphology via machine vision and learning algorithms. *Inventions*. <https://doi.org/10.3390/inventions9040080>
32. Zimmermann S, Griego D, Flatt RJ (2024) visualizing defects of concrete 3D printed structures with augmented reality based on machine learning-driven image analysis, p 150–157.
33. Rill-García R, Dokladalova E, Dokládal P, Caron J-F, Mesnil R, Margerit P, Charrier M (2022) Inline monitoring of 3D concrete printing using computer vision. *Addit Manuf* 60:103175. <https://doi.org/10.1016/j.addma.2022.103175>
34. Davtalab O, Kazemian A, Yuan X, Khoshnevis B (2022) Automated inspection in robotic additive manufacturing using deep learning for layer deformation detection. *J Intell Manuf* 33:771–784. <https://doi.org/10.1007/s10845-020-01684-w>
35. Kazemian A, Yuan X, Davtalab O, Khoshnevis B (2019) Computer vision for real-time extrusion quality monitoring and control in robotic construction. *Automat Constr* 101:92–98. <https://doi.org/10.1016/j.autcon.2019.01.022>
36. Jiang P, Ergu D, Liu F, Cai Y, Ma B (2022) A review of yolo algorithm developments. *Procedia Comput Sci* 199:1066–1073. <https://doi.org/10.1016/j.procs.2022.01.135>
37. Aljabri M, AlAmir M, AlGhamdi M, Abdel-Mottaleb M, Collado-Mesa F (2022) Towards a better understanding of annotation tools for medical imaging: a survey. *Multimed Tools Appl* 81:25877–25911. <https://doi.org/10.1007/s11042-022-12100-1>
38. Bruno G, Antonelli D, Stadnicka D (2021) Evaluating the effect of learning rate, batch size and assignment strategies on the production performance. *J Ind Prod Eng* 38:137–147. <https://doi.org/10.1080/21681015.2021.1883133>
39. Seo H, Back S, Lee S, Park D, Kim T, Lee K (2020) Intra- and inter-epoch temporal context network (IITNet) using sub-epoch features for automatic sleep scoring on raw single-channel EEG. *Biomed Signal Process Control* 61:102037. <https://doi.org/10.1016/j.bspc.2020.102037>
40. Qian Y, Kawashima S (2018) Distinguishing dynamic and static yield stress of fresh cement mortars through thixotropy. *Cem Concr Comps* 86:288–296. <https://doi.org/10.1016/j.cemeconcomp.2017.11.019>
41. Liu G, Cheng W, Chen L (2017) Investigating and optimizing the mix proportion of pumping wet-mix shotcrete with polypropylene fiber. *Constr Build Mater* 150:14–23. <https://doi.org/10.1016/j.conbuildmat.2017.05.169>
42. De Schutter G, Feys D (2016) Pumping of fresh concrete: insights and challenges. *RILEM Tech Lett* 1:76–80. <https://doi.org/10.21809/rilemtechlett.2016.15>
43. Feys D, De Schutter G, Fataei S, Martys NS, Mechthatherine V (2022) Pumping of concrete: understanding a common placement method with lots of challenges. *Cem Concr Res* 154:106720. <https://doi.org/10.1016/j.cemconres.2022.106720>
44. Shao L, Feng P, Zuo W, Wang H, Geng Z, Liu Q, Miao C, Liu Z (2022) A novel method for improving the printability of cement-based materials: controlling the releasing of capsules containing chemical admixtures. *Cem Concr Comps* 128:104456. <https://doi.org/10.1016/j.cemconcomp.2022.104456>
45. Tao Y, Mohan MK, Rahul AV, Yuan Y, De Schutter G, Van Tittelboom K (2022) Stiffening controllable concrete modified with redispersible polymer powder for twin-pipe printing. *Cem Concr Res* 161:106953. <https://doi.org/10.1016/j.cemconres.2022.106953>
46. Ren Q, Jiang Z, Li H, Zhu X, Chen Q (2019) Fresh and hardened properties of self-compacting concrete using silicon carbide waste as a viscosity-modifying agent. *Constr Build Mater* 200:324–332. <https://doi.org/10.1016/j.conbuildmat.2018.12.163>

Publisher's Note Springer Nature remains neutral with regard to jurisdictional claims in published maps and institutional affiliations.

